17th World Conference on Earthquake Engineering, 17WCEE
Sendai, Japan - September 13th to 18th 2020

SHALLOW LARGE SLIP OF THE 2008 IWATE-MIYAGI INLAND EARTHQUAKE INFERRED FROM STRONG-MOTION RECORDS

K. Yoshida[(1)], K. Miyakoshi[(2)]

[(1)] *Senior researcher, Geo-Research Institute, yoshida@geor.or.jp*
[(2)] *Chief Researcher, Geo-Research Institute,ken@geor.or.jp*

Abstract

In 14 June 2008, Mj7.2 earthquake was occurred around the border of Iwate and Miyagi prefecture, Japan. Some surface ruptures are found along the eastern margin of the aftershock area by previous studies. We investigated source process by inverting strong ground motion records. Assumed fault plane for our inversion was single west-dipping reverse fault. The velocity structure models used in this study were estimated by using waveform modeling of moderate earthquakes that occurred in the source region. The waveform inversion was conducted by using velocity waveforms recorded at 19 near-source strong-motion stations of K-NET, KiK-net, Japan Meteorological Agency and dam site. The source model indicated 3.4×10^{19} Nm of the total moment release, and a large slip area with an average slip of 3.1 m which is located in the southern shallow part of the hypocenter. This large slip area distributes in a depth between about 1 km (top of the assumed fault plane) and 5 km. The velocity seismogram recorded near the large slip area, is strongly affected from the shallow part (depth < 2 km) of the large slip area. In addition, distribution of the surface ruptures seems to be correlated to the large slip area. Calculated crustal deformation in the east of the source area from the estimated source model agrees with the observed one from InSAR data. Results of calculation of crustal deformation for various slip models indicated that the deformation of the east of the fault is controlled by the shallow part (depth < 2 km) of large slip area.

Keywords: Source inversion, 2008 Iwate-Miyagi Inland earthquake, Asperity, Shallow Fault Slip

1. Introduction

The 14 June 2008 magnitude 7.2 (JMA) Iwate-Miyagi Inland earthquake occurred on a fault near the border of Iwate and Miyagi prefecture, Japan. Recent dense strong-motion seismometer network recorded ground-motion during the 2008 earthquake and produced many near-fault strong motion data. The earthquake generated the strongest acceleration of 4-g ground-motion which has ever been recorded in the world at the IWTH25 KiK-net station [1]. Moreover, several strong-motion stations located near the fault recorded more than 1g accelerations and 60 cm/s velocities.

This earthquake is associated with surface ruptures on the east of the fault [2]. GNSS recordings and satellite image indicate clear crustal deformation occurred by earthquake [3, 4]. The surface ruptures and the crustal deformation suggest that the fault slip of this event extends to the Earth's surface. Significant static displacements are obtained from double integration of the strong motion acceleration records [e.g., 5]. These dense data of the earthquake are suitable to discuss shallow fault slip and near-fault ground motion.

In this study, we make a kinematic source model using the near-fault records, and discuss shallow fault slip. For this earthquake, several previous studies have proposed kinematic source models for long-period (< 1 Hz) ground motion [5, 6]. After these studies, strong motion records on the Aratozawa (ART) and Ishibuchi (ISB) dams which located near the fault plane (Fig. 1) have published. We analyze a kinematic source model using these new data with considering shallow fault slip.

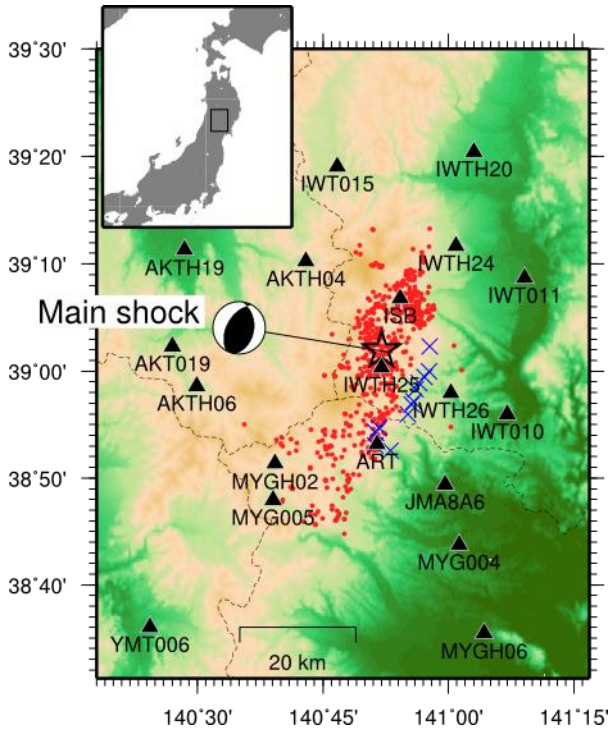

Fig. 1 Map showing stations used to analyze rupture models. Dots show epicenters of aftershocks that occurred within 24 hours after the mainshock [7]. Blue cross shows surface ruptures [2].

2. Velocity Model

In order to obtain accurate Green's functions, we used an inverse scheme to determine a set of 1D stratified velocity models adapted to each station. Several previous studies [8, 9, 10] constructed proper layered structure models to each station based on the waveform modeling of small events and succeeded in obtaining the detailed source rupture process. In this study, one-dimensional velocity model for each station are prepared following [11].

The waveform inversion method is a downhill-simplex method [12] for the Earth structure, which is parameterized as a layered medium with P- and S-velocities. The initial model was taken from the structure at the site location of the J-SHIS model. The objective function is defined by

$$f = \sum_{i=1}^{M}(O_i - C_i)^2 / \sum_{i=1}^{M} O_i^2 + p \quad (1)$$

where i is time, M is a number of sample, C_i is synthetic seismogram which is calculated using the discrete wavenumber method[13] and the Reflection/Transmission coefficient matrix method[14], and O_i is observed seismogram. p is a penalty parameter, which constrains Vp/Vs ratio, defined by

$$p = \gamma \sum_{j=1}^{L}\left(\alpha_j / \alpha_j' - 1\right)^2 \quad (2)$$

where, α_j is P-wave velocity at layer j; α_j' is the P-wave velocity calculated from the S-wave velocity at layer j using the empirical P- and S-wave velocity relation, which was derived from deep borehole logging data in Japan [15], and γ is the weight of the constraint.

Velocity models were inverted with fixed point source parameters and layer thicknesses using strong-motion data from seven moderate-magnitude earthquakes within the rupture area of the main shock (Fig. 2). The target acceleration seismograms were bandpass filtered between 0.2 Hz and 1.0 Hz and were integrated into velocities. The focal mechanism and seismic moment provided by F-net were used. The inverted velocity structure models are shown in Fig. 3.

In order to examine the appropriateness of the inverted velocity structure model, we simulated the waveforms of the A5 (Mw4.6) earthquake (Fig. 1) assuming a point source with a rise time of 0.35 s. The observed and synthetic velocity waveforms band-pass filtered between 0.2 Hz and 1 Hz are compared in Fig. 4. The synthetic waveforms using the inverted velocity structure models shown in Fig. 3 reasonably explain the observed waveforms.

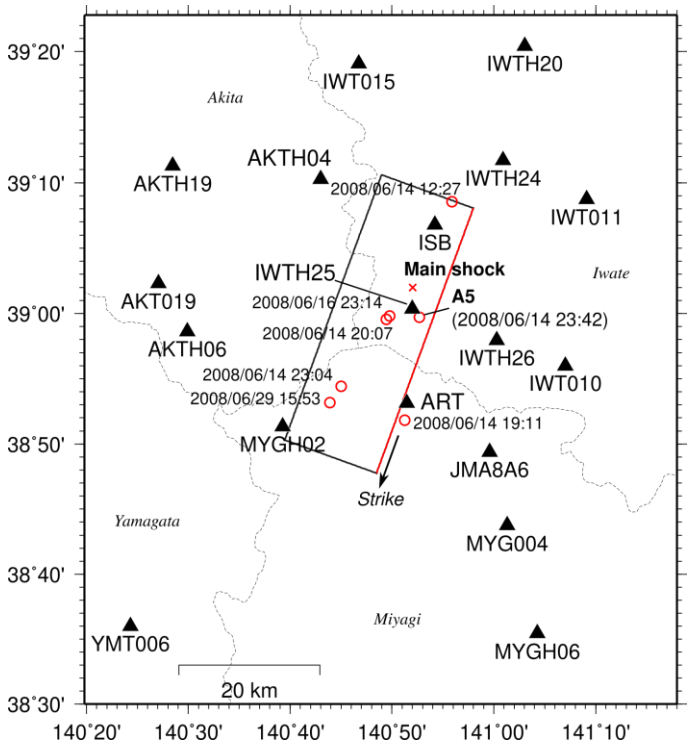

Fig. 2 Map showing aftershocks and stations used in the velocity model inversion. Black and red rectangular indicates projection of an assumed fault plane for the inversions. Cross indicates the location of the surface rupture associated with the earthquake [2]. A5 indicates the epicenter of the event in Fig. 4.

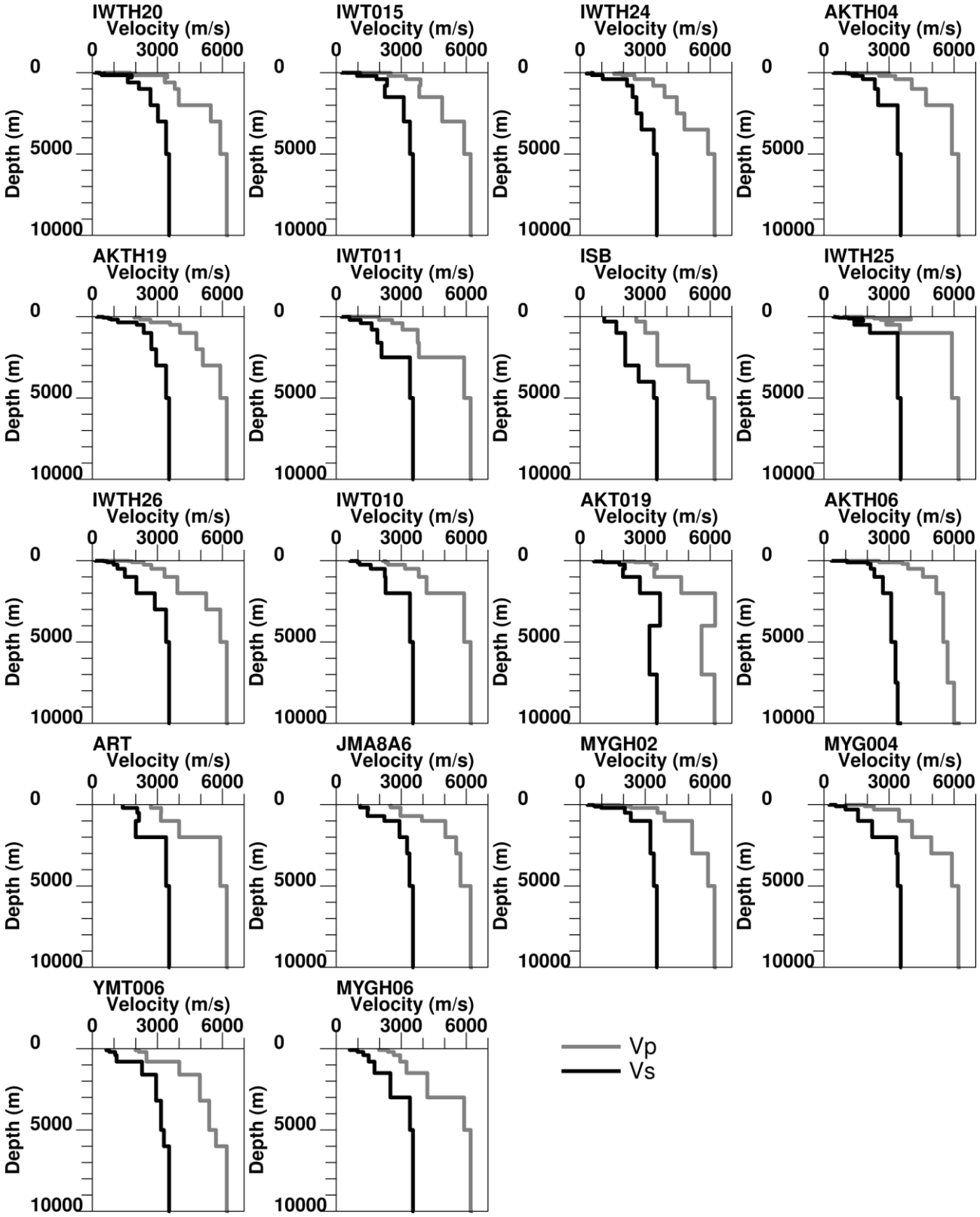

Fig. 3 Estimated velocity structure models.

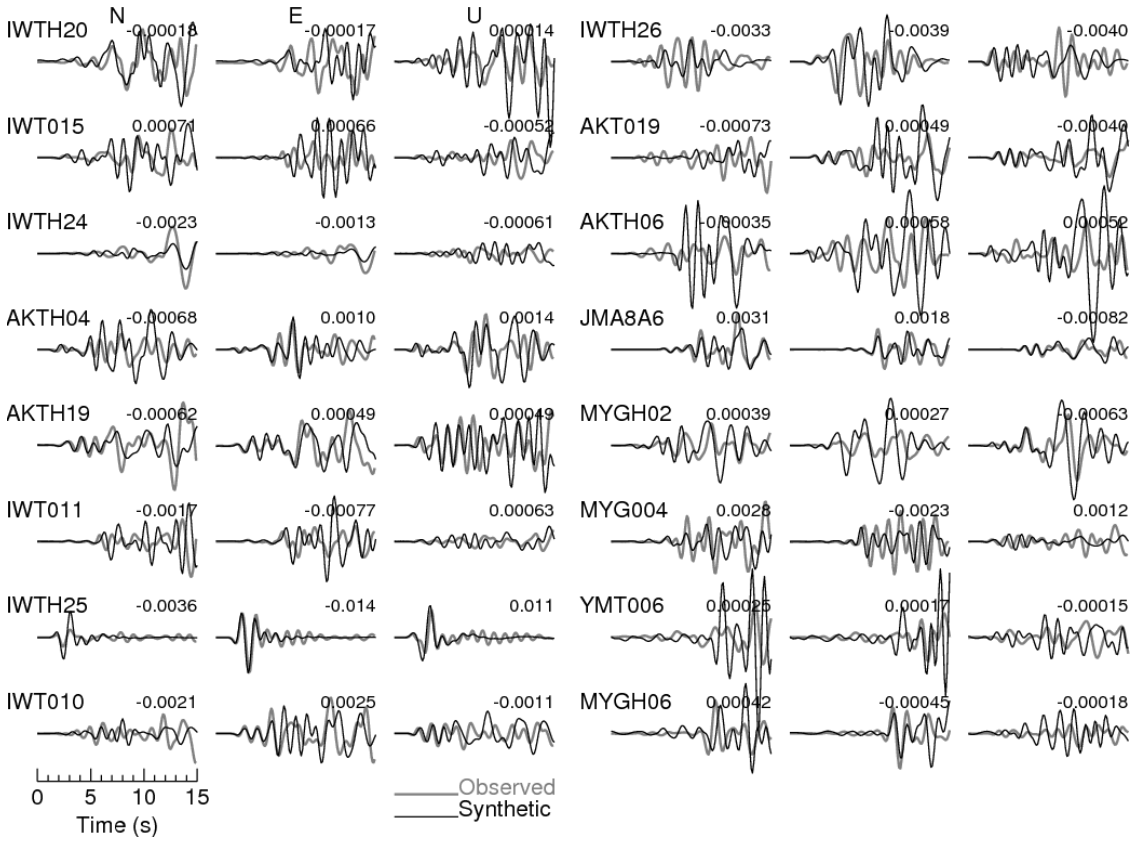

Fig. 4 Comparison of the observed and synthetic velocity waveforms (0.2-1.0 Hz) for the aftershock (A5).

3. Source Model

We performed waveform inversions for west-dipping single planar fault. Assumed fault plane was taken from the aftershock distribution determined from double-difference analysis of dense observation network data [7] (Fig. 2). The dimension of the fault plane is 42 km along strike and 16 km along dip. The strike and dip angles are N200° E and 40°, from the aftershock distribution [7]. Note that some researches proposed conjugate fault pair model for this event. This will be discussed in later section.

We applied multi-time-window linear waveform inversion procedure [16] to estimate the rupture process. We used the near-fault strong-motion data obtained from 15 stations of K-NET and KiK-net (borehole data used), 1 station of JMA (Japan Meteorological Agency), and 2 stations of dam site (ART and ISB). The data were windowed for 30 s, starting at P-wave arrival time, and band-pass-filtered between 0.05 to 1 Hz (period of 1-20 s) for waveform inversion. The accelerograms were integrated into ground velocities with a sampling frequency of 8 Hz.

Theoretical Green's functions were calculated using the discrete wavenumber method [13] and the Reflection/Transmission coefficient matrix method [14] using the 1D layered medium estimated in the section 2. In the multi-time window linear waveform inversion procedure, the moment-release distribution was discretized in both space and time. The fault plane was divided by a 2-km square subfault into 22 along strike and eight along dip. We distributed four point sources at a 667 m interval inside each subfault to consider the rupture propagation effect [17]. We aligned 14 smoothed ramp function having duration of 1.8 s at an interval of 0.9 s. This allows 6.8-s moment release for each subfault at a maximum. The weight of the smoothing constraint for inversion with a certain V_{FT} value was determined based on Akaike's Bayesian Information Criterion (ABIC) [18] following the previous studies [e.g., 19], and the inversion solution that gave the minimum misfit among those with different V_{FT} was selected as the best model.

Table 1 summarizes the inversion result. The total moment release was 3.4×10^{19} Nm, and the estimated average slip of the entire fault was 1.7 m. V_{FT} was searched in the range of 2.4–3.2 km/s and was determined to be 2.6 km/s by the minimum ABIC.

Final slip distribution is shown by Fig. 5a. The largest slip is 5.9 m at the southern shallow part of the hypocenter. The rigidity to obtain slip on the subfault from subfault moment release is obtained from the velocity model. We assumed Vs_1=2.7 km/s for the shallow layer (corresponds to the shallowest subfault) of the fault plane, which is discussed in later section. The final slip distribution shows that a large slip area on the southern shallow part of the fault (A1) was found (Fig. 5a). This large slip area corresponds to the asperity region defined by Somerville's criterion [20]. The average slip of A1 region is 3.1 m.

Comparison between the observed and synthetic velocity waveforms is shown by Fig. 6. In appearance, the synthetic waveforms agreed with the observed ones, excepted at some stations. Although we have not used displacement waveforms to fit, the synthetic displacement waveforms also agree with the observed displacement obtained from double-integration of the acceleration record with baseline correction [21] (Fig. 7). Contributions of the A1 on the ground motions (Fig. 6) showed that radiated waves from the A1 dominated the synthetic ground motions on the stations around the east and west of the fault plane (middle column in the Figure). In particular, the shallowest sufaults of A1 region (A1S) significantly affects to the velocity waveforms near the A1 area, e.g. ART and IWTH26D.

Distribution of peak of moment rate function are shown in Fig. 5b. We identified a high peak moment-rate area (hereafter HRA) by a similar procedure to identify asperities [20]. In this procedure, we used peak moment rate distribution instead of a slip distribution in order to determine the high rate region. Two HRAs were identified; one (H1) is near region to the asperity and another (H2) is on the south part of the fault. The H1 region is located on the similar area of the A1 asperity region. However, the A1S (the shallowest subfaults of the A1 asperity) region do not include in the HRA region. Moment rate functions of the shallow subfaults in the asperity region show long durations (=large slip) and somehow low peaks (=slow slip rate) than the ones of the deeper subfaults in the HRA. The slow and large slip in the shallow region suggested that ruptures in this region was dominated by frictions in the shallow weak zone [22].

H2 region may contribute strong motion for the southern stations. However, we focused on the surface rupture and shallow fault slip and did not argue this region in this study.

Table 1 Estimated fault parameters.

M_0 (Nm)	Mw	V_{FT} (km/s)	Max slip (m)	Average slip (m)
3.5×10^{19}	7.0	2.6	5.9	1.7

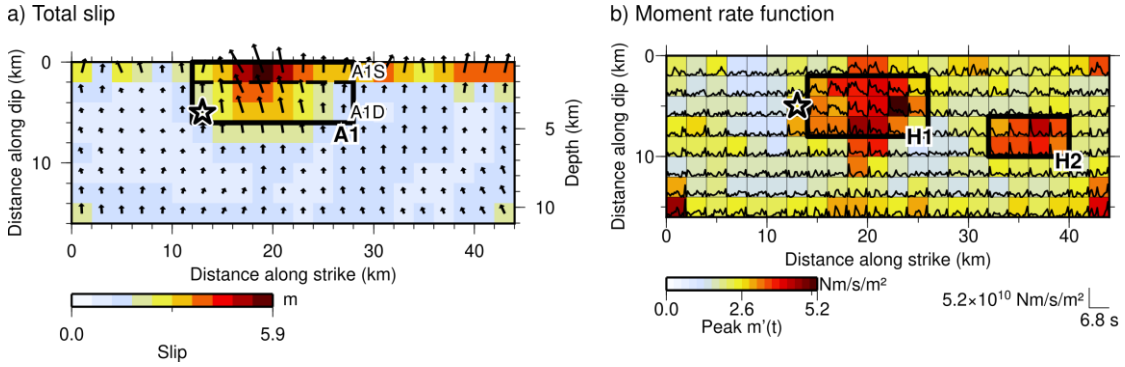

Fig. 5 a) Estimated total slip distributions. Star indicates the rupture starting point. Arrows show the amplitude and direction of slip. b) Estimated moment-rate density function. Backgrounds show the peak moment-rate density distributions.

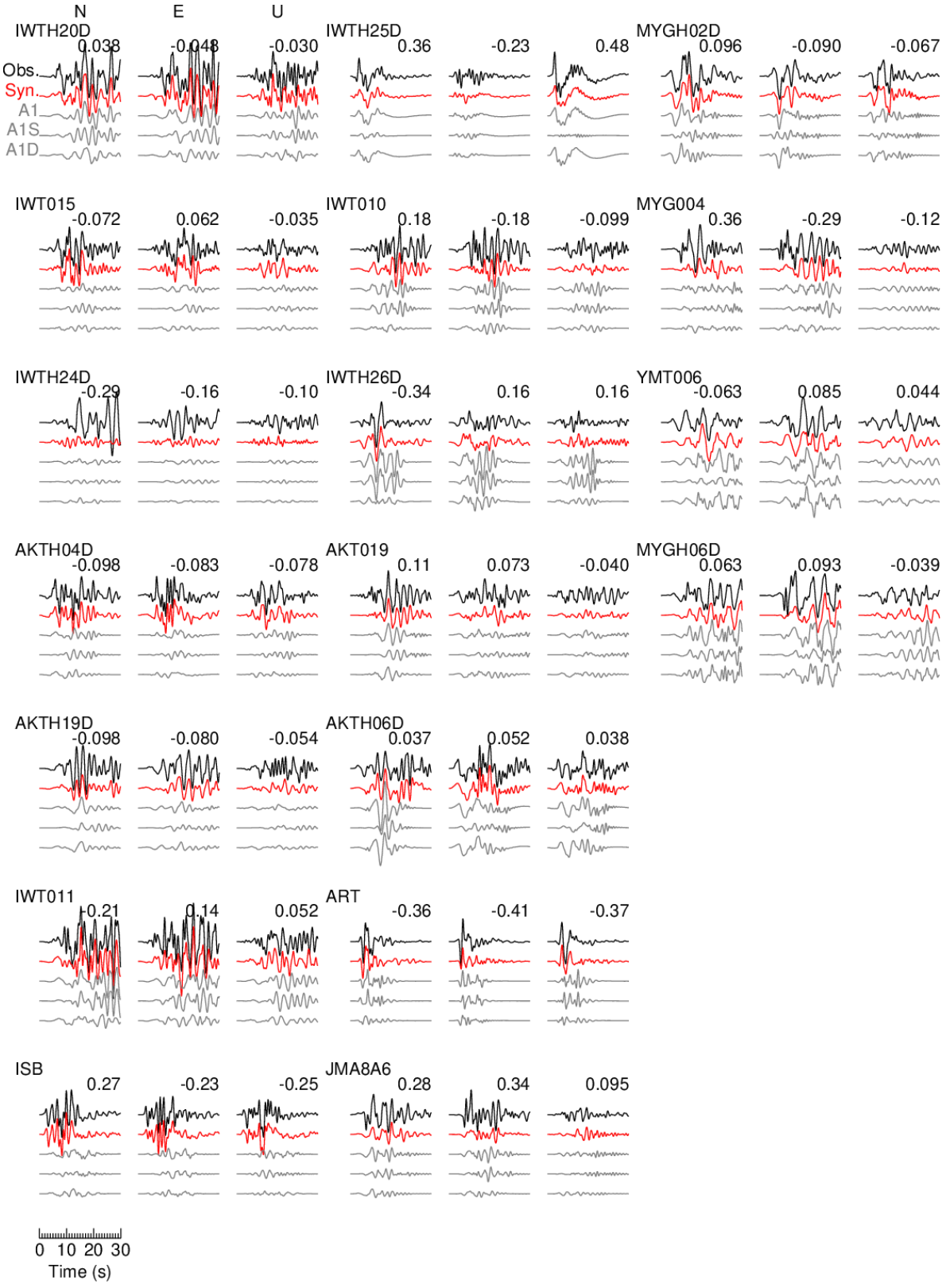

Fig. 6 Comparison between the observed (black) and synthetic (red) velocity waveforms. Maximum values for each component are indicated in the upper-right of each trace in m/s.

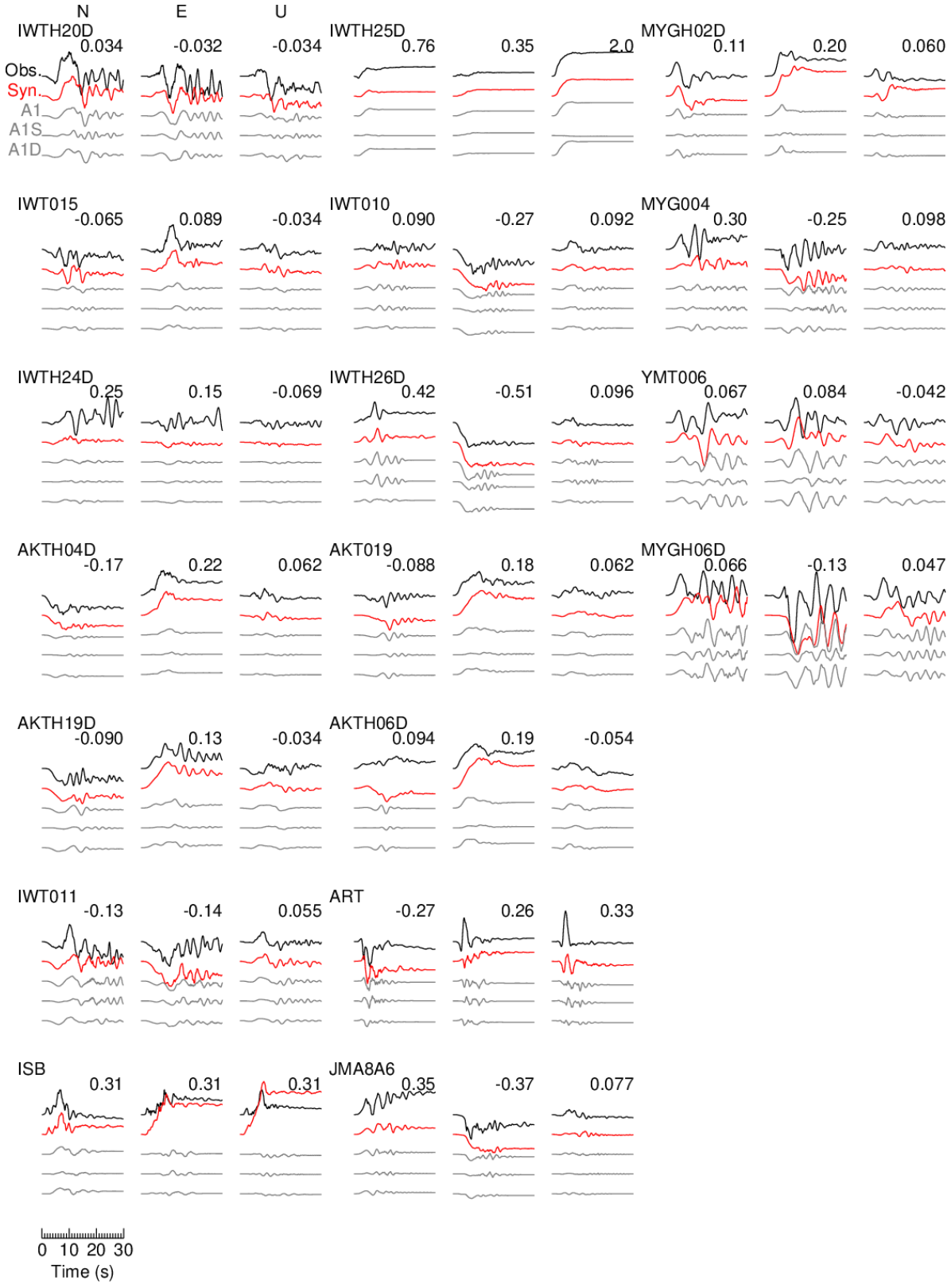

Fig. 7 Comparison between the observed (black) and synthetic (red) displacement waveforms. Maximum values for each component are indicated in the upper-right of each trace in m.

4. Shallow fault slip

The slip distribution is calculated from a subfault moment obtained from the inversion analysis and rigidity. Cross section of the J-SHIS v2 velocity structure model (Fig. 8) indicates that the top of the fault plane is shallower than the bedrock (Fig. 9). The structure model indicates that depth of the seismic bedrock varies steeply around the fault plane. The velocity models at IWTH25 and IWTH26 (Fig. 5) also imply that velocity in the shallow layer (layers above the seismic bedrock) changes between these sites. This steep changes make it difficult to determine appropriate S-wave velocity and density to calculate slip.

We determined amount of the shallow fault slip from the static displacement of nearby seismic stations (Fig. 8) obtained from double integration of the acceleration records (Fig. 7). Theoretical static crustal deformations caused by various fault slip were calculated for various models of shallow-layer S-wave velocity (Vs_1=2.1, 2.5, 2.7, 3.0, 3.4 km/s) by using [23]. The slip on the shallowest subfault (subfault mesh denoted as 1 in Fig. 9) was affected by V_{S1}. Comparison of the observed (from double integrated acceleration) and the calculated (from source model) static displacements at four stations indicates significant displacement contribution from the A1S region (Fig. 5) that is shallow part of A1 above the seismic bedrock (Fig. 10). This figure indicates that the calculated displacements increase as the Vs_1 decreases. Although the calculated displacement for IWTH26 agree with Vs_1=2.5 km/s model, the observations of IWTH010 and JMA8A6 is smaller than the calculations from the Vs_1=3.4 km/s model. Here, we adopted the Vs_1=2.7 km/s model considering balance of misfit. The total slip distribution shown in Fig. 5 was calculated by using Vs_1=2.7 km/s model.

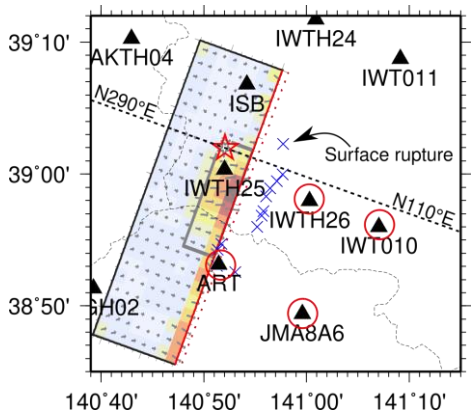

Fig. 8 Map showing the fault plane (solid rectangle) with slip distribution and seismic station (triangle). Red circle indicates the station used in the static displacement analysis shown in Fig. 10. Solid red line of the rectangle indicates upper side of the fault plane. Dashed red line indicates extension of the fault plane to the surface. Red star indicates the hypocenter. Dashed black line indicates the velocity profile shown in Fig. 9.

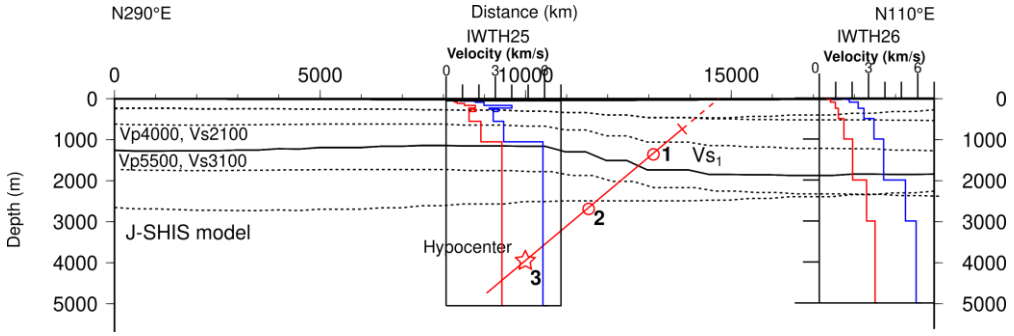

Fig. 9 Velocity structure model of J-SHIS across the fault plane. Solid line indicates seismic bedrock (Vs>3 km/s) and dashed line indicates layer boundary. Red line indicates the shallow part of the assumed fault plane. Red circle with number indicates the center of subfault mesh. The velocity model at IWTH25 and IWTH26 stations shown in Figure 3 are superimposed.

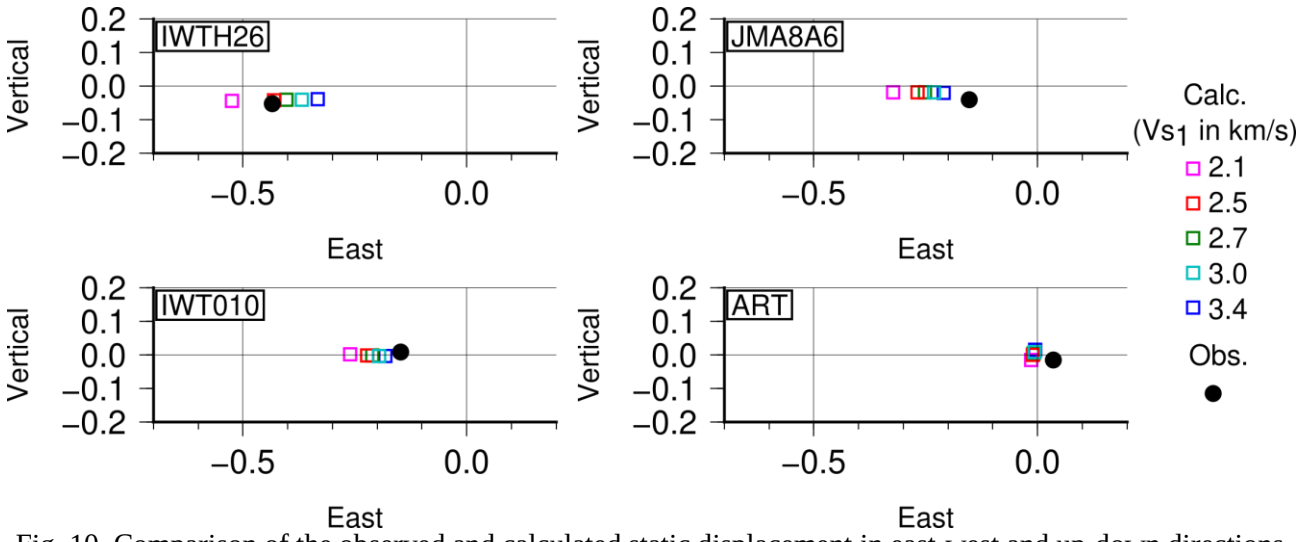

Fig. 10 Comparison of the observed and calculated static displacement in east-west and up-down directions for each station. The static displacements were calculated for various S-wave velocity in the shallow layer. Note that the seismometer of ART has no DC response.

5. Discussion

We calculated theoretical interferograms for crustal deformations caused by the slip distribution model assuming half-space elastic medium [23]. In Fig. 11, two interferograms calculated from slip models assuming different shallow velocities (Vs_1=2700 m/s and 3400 m/s) discussed in the previous section are shown. Compared to the result assuming Vs_1=3400 m/s, the computed interferograms assuming Vs_1=2700 m/s indicate large deformation (many fringes) on the eastern part of the fault plane caused by west-dipping reverse fault, and agree with the observed one.

Complex fault planes of this event could be recognized from Fig. 11. Different fringe pattern in the western side of the assumed fault plane between the observation and synthetics suggests an existence of additional slips on other fault planes. The aftershock distribution [7] showing east- and west-dipping patterns suggests that this event occurred on the complex conjugate fault system. Analyses of crustal deformations [4, 24] also indicate the conjugate fault system. These researches suggests that inversion analysis considering the complex fault system is needed to investigate the entire of source rupture model. Nevertheless, the large slip region associated with the surface ruptures on the eastern side of the fault plane was explaining in this study.

Acknowledgements

We used data provided from K-NET, KiK-net, and F-net. This study was based on the 2014 and 2015 research project “Improvement for uncertainty of strong ground motion prediction” by the Nuclear Regulation Authority (NRA), Japan.

Reference

[1] Aoi S, Kunugi T, Fujiwara H (2008): Trampoline Effect in Extreme Ground Motion. *Science*, **322**, 727-730.

[2] Toda S, Maruyama T, Yoshimi M, Kaneda H, Awata Y, Yoshioka T, Ando R (2010): Surface Rupture Associated with the 2008 Iwate-Miyagi Nairiku, Japan, Earthquake and its Implications to the Rupture Process and Evaluation of Active Faults. *Zisin 2*, **62**, 153-178. *in Japanese with English abst*.

[3] Takada Y, Kobayashi T, Furuya M, Murakami M (2009): Coseismic displacement due to the 2008 Iwate-Miyagi Nairiku earthquake detected by ALOS/PALSAR: preliminary results. *Earth Planet Space*, **61**, e9-e12.

[4] Ohta Y, Ohzono M, Miura S, Iinuma T, Tachibana K, Takatsuka K, Miyao K, Sato T, Umino N (2008): Coseismic fault model of the 2008 Iwate-Miyagi Nairiku earthquake deduced by a dense GPS network. *Earth Planet Space*, **60**, 1197-1201.

[5] Yokota Y, Koketsu K, Hikima K, Miyazaki S (2009): Ability of 1-Hz GPS data to infer the source process of a medium-sized earthquake: The case of the 2008 Iwate-Miyagi Nairiku, Japan, Earthquake. *Geophys. Res. Lett.*, **36**, L12301.

[6] Suzuki W, Aoi S, Sekiguchi H (2010): Rupture Process of the 2008 Iwate-Miyagi Nairiku, Japan, Earthquake Derived from Near-Source Strong-Motion Records. *Bull. Seism. Soc. Am.*, **100**, 256-266.

[7] Okada T, Umino N, Hasegawa A, Group for the aftershock observations of the Iwate-Miyagi Nairiku Earthquake in 2008 (2012): Hypocenter distribution and heterogeneous seismic velocity structure in and around the focal area of the 2008 Iwate-Miyagi Nairiku Earthquake, NE Japan − Possible seismological evidence for a fluid driven compressional inversion earthquake. *Earth Planet Space*, **64**, 717-728.

[8] Ichinose GA, Thio HK, Somerville PG, Sato T, Ishii T (2003): Rupture process of the 1944 Tonankai earthquake (Ms 8.1) from the inversion of teleseismic and regional seismograms. *J. Geophys. Res.*, **108**(B10), 2497.

[9] Asano K, Iwata T. (2009): Source Rupture Process of the 2004 Chuetsu, Mid-Niigata Prefectue, Japan, Earthquake Inferred from Waveform Inversion with Dense Strog-Motion Data. *Bull. Seism. Soc. Am.*, **99**, 123-140.

[10] Hikima K, Koketsu K. (2005): Rupture processes of the 2004 Chuetsu (mid-Niigata prefecture) earthquake, Japan: A series of events in a complex fault system. *Geophys. Res. Lett.*, **32**(18), L18303.

[11] Yoshida K, Miyakoshi K, Somei K, and Irikura K. (2017): Source process of the 2016 Kumamoto earthquake (Mj7.3) inferred from kinematic inversion of strong-motion records. *Earth Planet Space*, **69**, 64.

[12] Nelder JA, Mead R (1965): A simplex method for function minimization. *The Computer Journal*, **7**, 308-313.

[13] Bouchon M (1981): A Simple Method to Calculate Green's Functions for Elastic Layered Media. *Bull. Seism. Soc. Am.*, **71**, 959-971.

[14] Kennett B. L. N, Kerry N. J. (1979): Seismic waves in a stratified half space. *Geophys. J. R. Astr. Soc.*, **57**, 557-583.

[15] Kitsunezaki C, Goto N, Kobayashi Y, Ikawa T, Horike M, Saito T, Kurota T, Yamane K, Okuzumi K. (1990): Estimation of P- and S-Wave Velocities in Deep Soil Deposits for Evaluating Ground Vibrations in Earthquake. *J. JSNDS*, **9-3**, 1-17.

[16] Hartzell SH, Heaton TH (1983): Inversion of Strong Ground Motion and Teleseismic Waveform Data for the Fault Rupture History of the 1979 Imperial Valley, California, Earthquake. *Bull. Seism. Soc. Am.*, **73**, 1553-1583.

[17] Wald DJ, Helmberger DV, Heaton TH (1991): Rupture model of the 1989 Loma Prieta earthquake from the inversion of strong-motion and broadband teleseismic data. *Bull. Seism. Soc. Am.*, **81**, 1540-1572.

[18] Akaike H, (1980): *Likelihood and The Bayes procedure*. University Press, Valencia, Spain.

[19] Sekiguchi H, Irikura K, Iwata T (2000): Fault Geometry at the Rupture Termination of the 1995 Hyogo-ken Nanbu Earthquake. *Bull. Seism. Soc. Am.*, **90**, 117-133.

[20] Somerville PG, Irikura K, Graves R, Sawada S, Wald D, Abrahamson N, Iwasaki Y, Kagawa T, Smith N, Kowada A (1999): Characterizing Crustal Earthquake Slip Models for the Prediction of Strong Ground Motion. *Seism. Res. Lett.*, **70**(1), 59-80.

[21] Iwan WD, Moser MA, Peng C-Y (1985): Some observations on strong-motion earthquake measurement using a digital accelerograph. *Bull. Seism. Soc. Am.*, **75**, 1225-1246.

[22] Pitarka A, Dalguer LA, Day SM, Somerville PG, Dan K (2009): Numerical Study of Ground-Motion Differences between Buried-Rupturing and Surface-Rupturing Earthquakes. *Bull. Seism. Soc. Am.*, **99**, 1521-1537.

[23] Okada Y (1992): Internal deformation due to shear and tensile faults in a half-space. *Bull. Seism. Soc. Am.*, **82**, 1018-1040.

[24] Abe T, Furuya M, Takada Y (2013): Nonplanar Fault Source Modeling of the 2008 Mw6.9 Iwate-Miyagi Inland Earthquake in Northeast Japan. *Bull. Seism. Soc. Am.*, **103**, 507-518.

[25] Amagai T, Suzuki A, Wada K, Fujiwara M, Tobita M, Yarai H (2008): Detection of Crustal and Ground Deformation Triggered by the Iwate-Miyagi Nairiku Earthquake in 2008 with InSAR. *Journal of the Geographical Survey Institute*, **117**, 15-20.

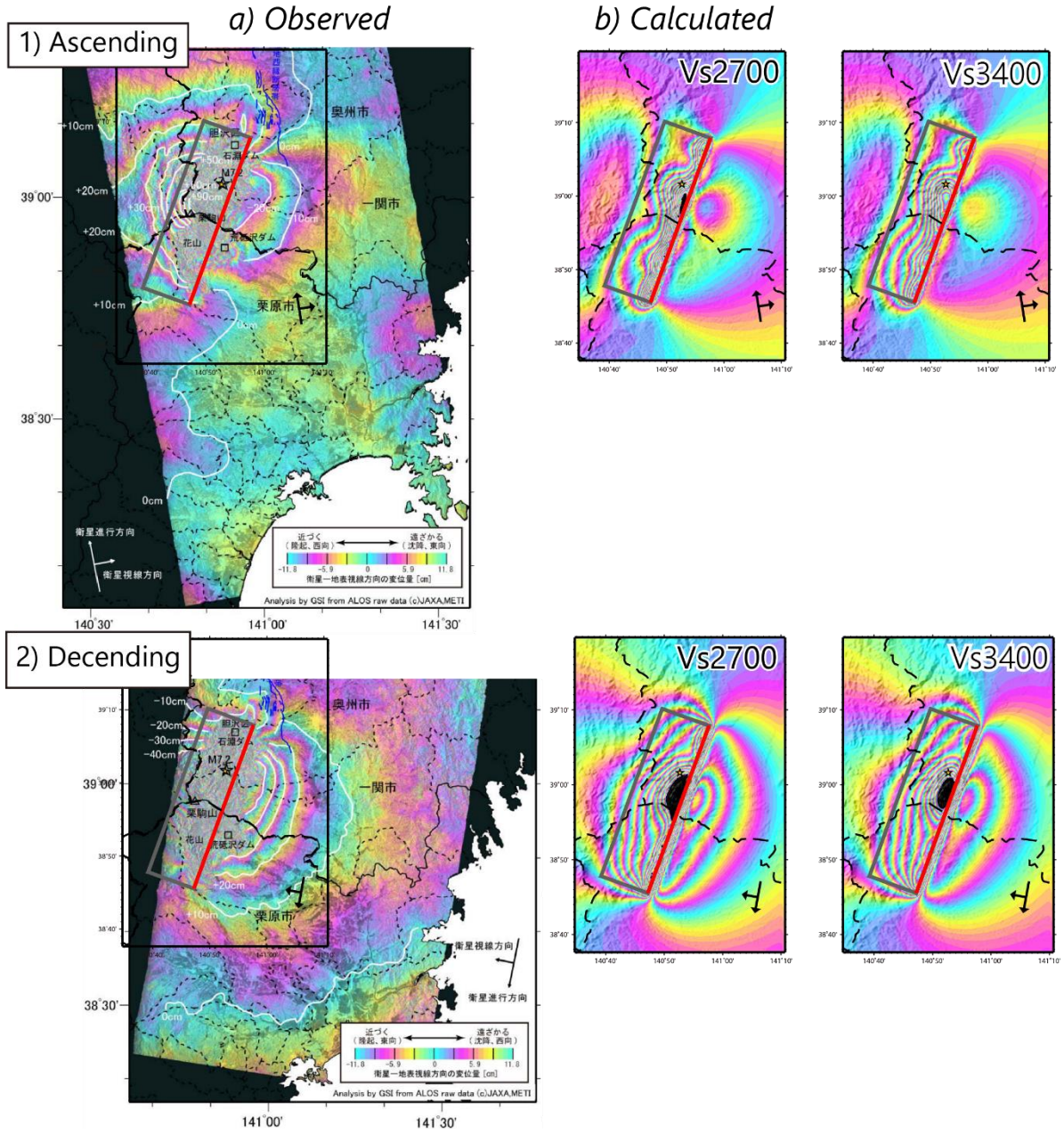

Fig. 11 Comparison of (left) observed [25] and (right) calculated interferograms from InSAR. Theoretical interferograms were calculated for the slip models converted from the moment release distributions assuming shallow Vs as Vs=2700 m/s and Vs=3400 m/s.

